IEEE Access
Multidisciplinary | Rapid Review | Open Access Journal

Received 28 February 2025, accepted 4 March 2025, date of publication 10 March 2025, date of current version 26 March 2025.

Digital Object Identifier 10.1109/ACCESS.2025.3549426

RESEARCH ARTICLE

Signal-to-Interference-Noise-Ratio Density Distribution for UAV-Carried IRS-to-6G Ground Communication

CHRISTANTUS OBINNA NNAMANI[1], (Member, IEEE), CHIDERA LINDA ANIOKE[2], SABA AL-RUBAYE[3], (Life Senior Member, IEEE), AND ANTONIOS TSOURDOS[3]

[1]PNDC, University of Strathclyde, G68 0EF Cumbernauld, U.K.
[2]Department of Electronic Engineering, University of Nigeria, Nsukka, Enugu 410001, Nigeria
[3]Faculty of Engineering and Applied Sciences, Cranfield University, MK43 0AL Bedford, U.K.

Corresponding author: Saba Al-Rubaye (s.alrubaye@cranfield.ac.uk)

This work was supported by EPSRC Communications Hub for Empowering Distributed Cloud Computing Applications and Research (CHEDDAR) Project under Grant EP/X040518/1 and Grant EP/Y037421/1.

ABSTRACT This paper investigates the probability distribution of the signal-to-interference noise ratio (SINR) for a 6G communication system comprising a multi-antenna transmitter, an intelligent reflecting surface (IRS) and a remote receiver station. A common assumption in the literature is that the density distribution function for SINR and signal-to-noise ratio (SNR) of an IRS-to-ground communication follows a Rayleigh and Rician distribution. This assumption is essential as it influences the derivation of the properties of the communication system such as the physical layer security models and the designs of IRS controller units. Therefore, in this paper, we present an analytical derivation for the density distribution functions of the SINR for an IRS-to-6G ground communication ameliorating the typical assumptions in the literature. We demonstrated that the SINR density function of an IRS-to-6G ground communication contains a hypergeometric function. We further applied the derived density distribution function to determine the average secrecy rate for passive eavesdropping.

INDEX TERMS IRS, 6G, density functions, SINR, UAV, antenna, physical layer security.

I. INTRODUCTION

The ability to support emerging wireless communication services with very high quality of service (QoS) requirements, artificial intelligence (AI) based and decentralised processing has triggered the need for 6G communication. The 6G network is characterized by ultra-high speed, ultra-low latency, and unlimited accessibility for optimal performance [1]. Following the conventional understanding of wireless communications, these requirements of 6G require improved energy and spectral efficiencies and ubiquitous coverage. These are achieved by segregating and decentralising the open radio access network (ORAN) and the 6G core networks emphasising AI-based automation [2], [3], [4]. A key part of the ORAN architecture is the RAN intelligent controller (RIC) which hosts reconfigurable meta-surfaces or intelligent reconfigurable surfaces (IRS).

The IRS provides a solution to manipulate spectral efficiency ensuring reliable connection [5], [6]. IRS is an enabling technology that enhances the capabilities and performance of new and emerging communication systems [7]. Its application has been studied for unmanned aerial vehicles (UAVs) [8], [9], mobile cell edge computing [10], [11], localization [12], [13], vehicular communication [14] and wireless power transfer [10]. The IRS utilizes phase shifts of the reflection coefficients to control transmitted signal path, thereby maximizing achievable secrecy rates in UAVs [8] and spectral efficiency in mmWave/terahertz 6G communication [15], [16].

The massive low-cost reflecting elements independently alter the amplitude and phase of impinging waveforms via a software-controlled structure [17], [18]. A characteristic

The associate editor coordinating the review of this manuscript and approving it for publication was Barbara Masini.

of the IRS-assisted system is the possibility to transmit and receive signals within the same frequency band and time slot, i.e. full duplex mode. This property prevents self-interference and improves receiver performance [9]. In obstructed line-of-sight scenarios, the IRS can significantly improve the quality of the received signal through constructive super-positioning of impinging waves from each surface of the IRS [19].

Considering that wireless communication channels are stochastic, the impact of the IRS system relies on its ability to configure the random channel coefficients. Emphasizing spectral efficiency, the IRS impact defines how it affects the signal-to-interference-noise ratio (SINR). The effect of the random channel coefficients on the IRS introduces a probabilistic model to the IRS control and settings. This probabilistic model for the IRS impact is essential in determining its characteristics like the average secrecy rate, and the AI-based state transition controller design in 6G. In literature, the probabilistic model is assumed to be Rayleigh distributed [16], [20] and/or Rician distributed [5]. In this paper, we presented a novel determination of the density distribution of an IRS-to-6G ground station to ameliorate the probabilistic model assumption. The primary objectives are as follows:

1) To derive the SINR density distribution function for an IRS-to-6G ground communication system using analytical methods. It is essential to consider that the interfering signals can be line-of-sight (LoS) and non-LoS (NLoS).
2) The application of the density distribution in determining the definition of average secrecy rate.

We note that while the derivations of this paper apply to 5G IRS systems, the simulation environment is configured using the 6G RIC infrastructure.

Notations: $\{\cdot\}^T$ and $\{\cdot\}^H$ represent the transpose and Hermitian of vectors/matrices, respectively, while $I_v(\cdot)$ is the v-order modified Bessel function of the first kind. $diag(x)$ is a diagonal matrix with x as the main diagonal and $\mathbb{E}[x]$ is the expected value of x. $\mathcal{R}_+$ represents positive real numbers.

II. RELATED WORKS

In this section, we discuss the literature and reviews related to this paper's principal focus. We begin by outlining the challenges of the IRS system based on the need for a density distribution study. We then discuss the literature defining SNR and finally emphasize the importance of applying the density distribution to determining physical layer characteristics.

A. CHALLENGES AND REQUIREMENTS FOR IRS

IRS employ passive beamforming with a gain dependent on accurate channel estimation. The IRS systems enable a wireless channel that can be altered dynamically to mitigate channel fading impairments [21]. However, knowledge of the wireless channel is required to manipulate the channel, creating a unique channel estimation problem. One of the channel estimation problems in IRS-enabled systems results from the inadequate signal processing capacity of its low-cost passive reflecting elements. Secondly, the IRS-enabled system relies on wireless communication and sensing for accurate recovery of the transmitted information and channel estimation [22]. Estimating a wireless channel relies on the probabilistic knowledge of its performance.

Additionally, the IRS system improves the reception of transmitted signals at legitimate or approved terminals while limiting unauthorized interception [8]. The exponential rise in new and emerging technologies increases the propensity for information theft. The evaluation of the secrecy metrics is usually complicated because of the introduction of additional information rate parameters and the configurations of the IRS system. The problems are generally non-convex with sub-optimal solutions. Nevertheless, the IRS reflection coefficient must be carefully designed to minimize information theft. Optimization problems for the IRS reflection coefficient have been treated in [8] and [23]. The secrecy computation depends on the probabilistic model of the SINR at the receivers.

B. ON PDF DETERMINATION FOR SINR FOR IRS-SYSTEM

Enhanced performance of IRS-assisted systems is essential in analyzing and maximizing the IRS system's performance metrics. Parameters such as the ergodic rate, outage capacity, bit error rate (BER), number size and placements of reflecting elements etc. rely on the probability model of the IRS system's interaction with the instantaneous random wireless channels [19]. In literature, it is common to assume varying distributions of large-scale and small-scale channel models such as the Rayleigh, Rician, Nakagami-m and Von Mises distribution to determine the PDF of the IRS-to-ground communications not specific to 6G.

The concept of determining the probabilistic model for the impact of the IRS system on wireless communication models is prevalent in the literature. For example, [24] examined the performance of IRS-aided downlink communication using non-orthogonal multiple access (NOMA) in Nakagami-m fading channels with co-channel interference (CCI). Considering that the distribution is a Gamma approximation function, it derived expressions for the ergodic capacity and outage probability. To maximize the SNR of IRS-assisted wireless systems, [25] designed the phase shift of each reflecting element while deriving an optimal reflection phase. The analysis in [25] showed that the SNR PDF follows a non-central Chi-square distribution if the signal power components are Rayleigh distributed. The relevance of the SNR distribution was applied to the determination of achievable rate and secrecy outage probability.

Furthermore, the statistical characterization of optimal SNR for a distributed IRS-aided system operating over Nakagami-m fading channels was evaluated in [26]. Reference [26] found closed-form expressions of the SNR to access system parameters like the SNR coverage probability. The effect on the SNR by controlling the phase shifts

of the distributed IRS system was quantified, and tight approximations of the PDF and CDF were also determined. In [27], the distribution of the SNR for an IRS-assisted single-input-single-output (SISO) system was determined by exploiting the central limit theorem and deriving closed-form expressions for the effective capacity.

In these formulations of the impact of IRS distribution, there is a common assumption that the noise and interfering signals do not influence the distribution. This has limited these studies to SNR. Specifically, in this paper, we studied the impact of the interfering signal on the IRS system by incorporating its density distribution. Without loss of generality, we assume that the interfering signals will have line-of-sight (LoS) and non-LoS (NLoS) impacts, hence we modelled them using a Rician distribution.

C. ON APPLICATION OF SINR PDF

The deployment of UAVs for communication is fast becoming a mainstream solution to provide access to rural and/or geographically difficult terrains [3], [20]. The accessibility to these terrains can be marred by man-made and natural causes. However, the UAV is a low-energy device with a battery system as its primary source of energy. This limited energy is mainly used for flight, thereby constraining the available energy for communication applications. Nevertheless, due to advances in technology, it has become somewhat more efficient to deploy UAVs as a relay node with passive communication equipment.

These passive technologies are becoming popular with the recent migration into the 6G communication. Predominately, the IRS system is a mainstay of the 6G infrastructure which is used to manipulate the communication channel by choosing appropriate reflection coefficients to maximize signal reception at desired locations [6], [15]. However, the reflections from the IRS are not specular due to the underlining characteristics of radio waves as discussed in [28]. This non-specularity leads to the possibility of eavesdropping albeit with weak signal reception at the eavesdropper.

In literature, the presence of an eavesdropper in communication from a multiple-input-single-output (MISO) system with a fixed IRS system has been studied [29]. Furthermore, [8], [30] examined the incorporation of the IRS system on a UAV. Notably, [30] did not consider the secrecy of the communication nor the source wireless sensor network thereby undermining the secured communication of the aerial system for typical IoT applications. Other studies of IRS designs in wireless communication include secrecy rate maximization [31], joint active and passive beamforming design [32], and rate region characterization for IRS-aided interference channels [33]. A distinct feature of these IRS implementations on UAV systems is the reliance on the assumption that the SINR is Rayleigh distributed. However, in this paper, we have demonstrated that the SINR contains a hypergeometric function, hence, we applied the distribution to determine the average secrecy rate of a UAV-mounted IRS system.

III. PROBLEM FORMULATIONS

Consider that a 6G ground transmitting base station (gNB) equipped with M multi-antennas sending messages (signals) through K elements IRS to a ground receiver at sub-THz (above 100GHz) frequency band. We note the consideration of a 6G transmission relies on the operating frequency which invariably reduces the penetration distance of the transmitted signal. The IRS may be placed on a ground-based stationary platform or an aerial system like a UAV as depicted in Fig. 1. We note that the primary emphasis of the density distribution is IRS placed on the fixed ground-based platform. However, the application of a UAV-carrying IRS system relies on the sampling approach of determining UAV trajectory and IRS parameters as presented in [6], [8], and [9]. The sampling method considers infinitesimal points where the IRS parameters were evaluated with the density distribution functions derived herein. Without loss of generality, we assume that in a 6G urban environment, the gNB does not have LoS propagation with the user. This assumption does not affect the probability formulations because the LoS component of the signal power can be summed as in [17] and evaluated using central limit theory (CLT). Given an instantaneous passband signal, $x(t)$, the received signal at a user receiver located at any ith geographical point is given as (1).

$$y_i = h_i^H \boldsymbol{\Theta} G w x(t) + \sum_{i=0}^{\infty} S_i \bar{x}(t) + n_i, \tag{1}$$

where $h_i = [h_{1i}, \ldots, h_{Ki}]^T \in \mathcal{C}^{K\times 1}$ and $G \in \mathcal{C}^{K\times M}$ are the complex channel matrices between the IRS system to the ith user, and the multi-antenna transmitter to the IRS system respectively. The symbol $w = [w_1, \ldots, w_M]^T$ is the vector of beamforming weights corresponding to the M radiation from each $m \in M$ antenna. The symbol $\boldsymbol{\Theta} = diag(\exp(j\theta_1), \exp(j\theta_2), \ldots, \exp(j\theta_K))$ represents the vector of the reflection coefficients (θ) from each IRS element while $n_i \sim \mathcal{CN}(0, \sigma_n^2)$ is an independent and identically distributed (i.i.d.) additive white Gaussian noise (AWGN). S_i represent infinitely sourced interfering signal power while $\bar{x}(t)$ is the interfering signal. Let us assume that the noise and interfering signals are additive with common distribution, such that their combined signal strength is $S_{n+int} = S_i + \sigma_n^2$. For ease of analysis, we assume that the noise and interfering signals are uncorrelated with independent sources and arrival paths. Therefore, the received signal-to-interference and noise ratio at any ith location is given as (2).

$$\gamma_i = \frac{|h_i^T \boldsymbol{\Theta} G w|^2}{S_{n+int}}. \tag{2}$$

The primary objective of this paper is to investigate and define the properties of the density distribution of (2) following the assumption that the interfering signal has LoS and NLoS components.

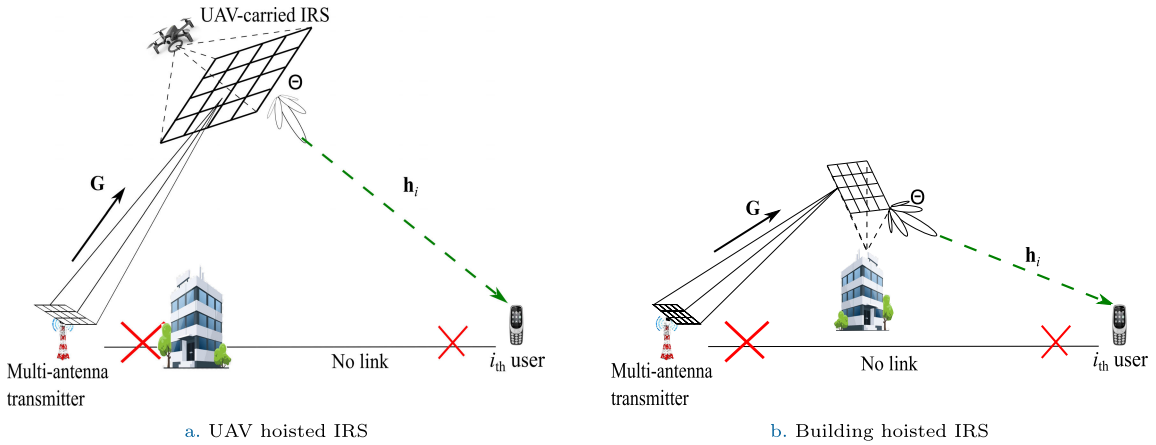

FIGURE 1. Schematic of a typical IRS-to-ground interaction.

IV. MODEL DESCRIPTION

Let $b = |h_i^T \mathbf{\Theta} G w|^2$ and $a = S_{n+int}$ representing uncorrelated randomly generated variable such that $\gamma_i = \frac{b}{a}$, $\forall\, a > 0$, $b \in [0, \infty)$. In this section, we describe the density functions of a and b.

A. INTERFERING SIGNALS DENSITY

We note that the interfering signals can have multiple unknown sources. For example, the destructive combination of the imperfectly blocked LoS link between the transmitting station and the users is shown in Fig. 1. Due to the random channel variations, we can consider the interfering signal, $S_{n+int} \in \mathcal{R}_+$, as a Rician distributed random variable with PDF given as (3) and location and scaling parameters of υ, and ϱ respectively. The choice of Rician distribution follows from its property to capture the line of sight (LoS) property of the signal, its non-LoS (NLoS) property and the statistical independence of the interfering signals. This will account for different types of interfering signals. The interference from the LoS part of the distribution constitutes slow-varying fading and depends on the receiver position. However, the NLoS components arise from fast varying fading and are caused by the multi-path effects [5]. Furthermore, the Rician distribution can easily be reduced to a Rayleigh distribution representing a typical wireless scenario by setting $\upsilon = 0$.

$$p_A(a) = \frac{a}{\varrho^2} e^{-\left(\frac{a^2+\upsilon^2}{2\varrho^2}\right)} I_0\left(\frac{a\upsilon}{\varrho^2}\right),\ \forall\, a > 0, \tag{3}$$

where $I_0(\cdot)$ is the zero-order modified Bessel function of the first kind and $\varrho > 0$. Figure 2 presents the shape of the distribution given in (3). The choice of location and scale parameters affects the type and magnitude of distribution. We note that the PDF of a Rician distribution can be written as a scaled non-central chi-squared distribution such that $p_A(a) = \frac{2a}{\varrho^2} f\left(x_a = \frac{a^2}{\varrho^2} \mid k = 2, \lambda = \frac{\upsilon^2}{\varrho^2}\right)$. It is known that the PDF of the non-central chi-squared distribution is presented in (4) and substituting the defined parameters of x_a, k, and λ

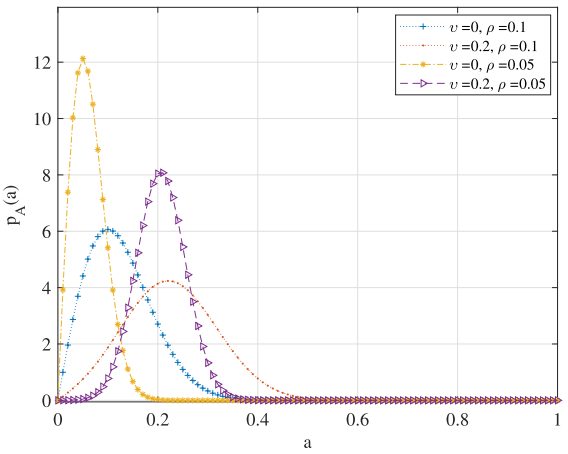

FIGURE 2. Impact of varying the location and scale parameters on the distribution in (3).

will give rise to (3).

$$f(x \mid k, \lambda) = \frac{1}{2} e^{-\left(\frac{x+\lambda}{2}\right)} \left(\frac{x}{\lambda}\right)^{\frac{k}{4}-\frac{1}{2}} I_{\frac{k}{2}-1}\left(\sqrt{\lambda x}\right) \tag{4}$$

B. DESIRED SIGNALS DENSITY

Following algebraic and matrix manipulations, we can write that $h_i^H \mathbf{\Theta} G w = \sum_{k=1}^{K} h_k \theta_k \sum_{m=1}^{M} G_{km} w_m$. Let $X_k = h_k \theta_k$ and $Y_k = \sum_{m=1}^{M} G_{km} w_m$ be independent and uncorrelated random variables. We note that the statistical independence of the random variables allows for the superposition of the signals arriving from each antenna element of the transmitter and the elements of the IRS system. By CLT, the PDF of $\sum_{k=1}^{K} X_k Y_k$ is Gaussian distributed with expected value and variance of $\mu = \mathbb{E}[KX_k]\mathbb{E}[Y_k]$ and $\sigma^2 = \mathbb{E}[KX_k^2 Y_k^2] - \mathbb{E}[X_k Y_k]^2$ respectively [34]. We note that the parameters μ and σ are expected values implying that they are weighted averages and do not necessarily have to increase/decrease by increasing/decreasing the number of IRS elements. By definition, taking the magnitude of a Gaussian random

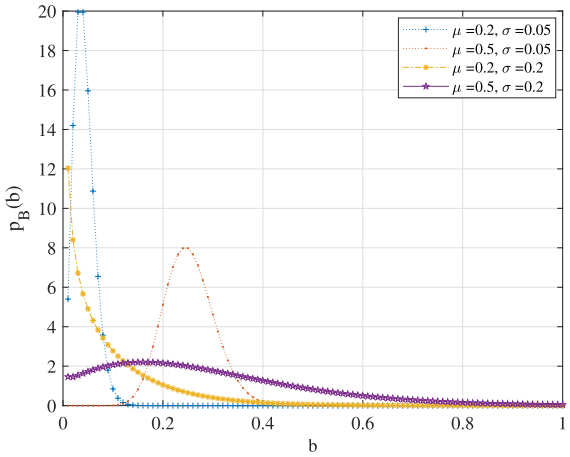

FIGURE 3. Impact of varying the location and scale parameters on the distribution in (8).

variable gives a folded normal distribution with location and scale parameters $\mu \in \mathcal{R}_+$ and $\sigma^2 > 0$ respectively. Invariably the squared of the folded normal distribution can be obtained using the transformation of random variables to arrive at (5) which is further simplified to (8) through the steps (6) and (7).

$$p_B(b) = \frac{1}{2\sqrt{b}\sqrt{2\pi\sigma^2}}\left(e^{-\left(\frac{(\sqrt{b}-\mu)^2}{2\sigma^2}\right)} + e^{-\left(\frac{(\sqrt{b}+\mu)^2}{2\sigma^2}\right)}\right) \quad (5)$$

$$p_B(b) = \frac{1}{2\sqrt{b\sigma^2}}e^{-\left(\frac{b+\mu^2}{2\sigma^2}\right)}\sqrt{\frac{2}{\pi}}\cosh\left(\frac{\mu\sqrt{b}}{\sigma^2}\right) \quad (6)$$

But $I_{-\frac{1}{2}}(x) = \frac{\sqrt{\frac{2}{\pi}}\cosh(x)}{\sqrt{x}}$ [35]

$$p_B(b) = \frac{1}{2\sqrt{b\sigma^2}}e^{-\left(\frac{b+\mu^2}{2\sigma^2}\right)}\sqrt{\frac{2}{\pi}}\sqrt{\left(\frac{\mu\sqrt{b}}{\sigma^2}\right)}I_{-\frac{1}{2}}\left(\frac{\mu\sqrt{b}}{\sigma^2}\right) \quad (7)$$

$$p_B(b) = \frac{1}{2\sigma^2}\sqrt{\frac{\mu}{\sqrt{b}}}e^{-\left(\frac{b+\mu^2}{2\sigma^2}\right)}I_{-\frac{1}{2}}\left(\frac{\mu\sqrt{b}}{\sigma^2}\right) \quad (8)$$

where $\sigma^2 > 0$ and $b > 0$. By the formulation of (8), $\mu > 0$ because of the presence of interference plus noise power. The impact of the location and scale parameters on the shape and magnitude of the distribution are visible in Fig. 3. Equation (8) is a scaled non-central chi-squared distribution, $f(x \mid k, \lambda)$, with a scaling parameter of $\frac{1}{\sigma^2}$. It has one degree of freedom and a non-centrality parameter $\lambda = \frac{\mu^2}{\sigma^2}$ with representation as given in (4), $p_B(b) = \frac{1}{\sigma^2}f\left(x_b = \frac{b}{\sigma^2} \mid k = 1, \lambda = \frac{\mu^2}{\sigma^2}\right)$.

V. DENSITY DISTRIBUTION FUNCTION

To determine the density function of $\gamma_i = \frac{b}{a}$, $\forall\, a > 0$, $b \in [0, \infty)$, we propose that given a is Rician distributed and b is a non-central chi-squared distribution, that the density function of γ_i is given as (9).

$$p_\gamma(\gamma_i) = \sum_{k=1}^{\infty} A_k \frac{\gamma_i^{\kappa-\frac{1}{2}}}{(\gamma_i+1)^{2\kappa+2}} {}_2F_1\left(-\kappa, \frac{1}{2}-\kappa; 1; \frac{\upsilon^2\sigma^2}{\mu^2\varrho^2\gamma_i}\right), \quad \forall\, \gamma_i > 0, \quad (9)$$

where $A_k = \frac{4\sqrt{2}e^{-\left(\frac{\mu^2}{2\sigma^2}+\frac{\upsilon^2}{2\varrho^2}\right)}\Gamma\left(\kappa+2\right)}{\kappa!\varrho\sigma^2\Gamma\left(\kappa+\frac{1}{2}\right)}\left(\frac{\mu^2}{\sigma^2}\right)^{\kappa}$, $\kappa = 2k-1$, the pair $\{\mu,\ \sigma\}$ and $\{\upsilon,\ \varrho\}$ are the locations and scales of b and a respectively. $\Gamma(.)$ and ${}_2F_1(.)$ represents the gamma and Gauss hypergeometric [36] functions respectively.

Proof: Consider that x_a and x_b are independent random variables, we rewrite (3) and (8) as a scaled non-central chi-squared distribution as given in (10) and (11) respectively. We note that $x_a = \frac{a^2}{\varrho^2}$ and $x_b = \frac{b}{\sigma^2}$ are statistically independent which allows the substitution of $a = \sqrt{x_a\varrho^2}$ and $b = x_b\sigma^2$. In practice the independence of x_a and x_b is assumed considering that the interfering signal source is not co-located with the source of the desired signal.

$$p_A(x_a) = \frac{\sqrt{x_a}}{\varrho}e^{-\left(\frac{x_a}{2}+\frac{\upsilon^2}{2\varrho^2}\right)}I_0\left(\frac{\upsilon}{\varrho}\sqrt{x_a}\right) \quad (10)$$

$$p_B(x_b) = \frac{1}{2\sigma^2}e^{-\left(\frac{x_b}{2}+\frac{\mu^2}{2\sigma^2}\right)}\left(\frac{\sigma^2x_b}{\mu^2}\right)^{-\frac{1}{4}}I_{-\frac{1}{2}}\left(\frac{\mu}{\sigma}\sqrt{x_b}\right) \quad (11)$$

Let z be a random variable with a one-to-one mapping to x_a. The PDF of γ_i is obtained by solving (12).

$$p_\gamma(\gamma_i) = \int_{-\infty}^{\infty} p_B(\gamma_i z)p_A(z)|z|dz. \quad (12)$$

$$p_\gamma(\gamma_i) = \int_{-\infty}^{\infty} \frac{1}{2\sigma^2}e^{-\left(\frac{\gamma_i z}{2}+\frac{\mu^2}{2\sigma^2}\right)}\left(\frac{\sigma^2\gamma_i z}{\mu^2}\right)^{-\frac{1}{4}}I_{-\frac{1}{2}}\left(\frac{\mu}{\sigma}\sqrt{\gamma_i z}\right) \times \frac{\sqrt{z}}{\varrho}e^{-\left(\frac{z}{2}+\frac{\upsilon^2}{2\varrho^2}\right)}I_0\left(\frac{\upsilon}{\varrho}\sqrt{z}\right)|z|dz. \quad (13)$$

$$p_\gamma(\gamma_i) = A(\gamma_i)\int_{-\infty}^{\infty} z^{\frac{5}{4}}e^{-\left(\frac{z(\gamma_i+1)}{2}\right)}I_{-\frac{1}{2}}\left(\sqrt{\frac{\mu^2\gamma_i}{\sigma^2}}\sqrt{z}\right) \times I_0\left(\sqrt{\frac{\upsilon^2}{\varrho^2}}\sqrt{z}\right)dz. \quad (14)$$

where $|z| = z$ and $A(\gamma_i) = \frac{1}{2\sigma^2\varrho}\left(\frac{\gamma_i\sigma^2}{\mu^2}\right)^{-\frac{1}{4}}e^{-\left(\frac{\mu^2}{2\sigma^2}+\frac{\upsilon^2}{2\varrho^2}\right)}$.

We note that

$$\int_{-\infty}^{\infty} f(z)dz = \underbrace{\int_{-\infty}^{0} f(z)dz}_{Part\ A} + \underbrace{\int_{0}^{\infty} f(z)dz}_{Part\ B},$$

where $f(z) = z^{\frac{5}{4}}e^{-\left(\frac{z(\gamma_i+1)}{2}\right)}I_{-\frac{1}{2}}\left(\sqrt{\frac{\mu^2\gamma_i}{\sigma^2}}\sqrt{z}\right)I_0\left(\sqrt{\frac{\upsilon^2}{\varrho^2}}\sqrt{z}\right)$. Therefore, we solve Part A and Part B using integration by substitution as follows:

1) Part A: Let $w = \sqrt{-z}$, we therefore have that $dz = -2wdw$ and $z = -w^2$ with integration boundary from

∞ to 0. However, by rearranging the integral function, we obtain

$$\int_{-\infty}^{0} f(z)dz \Rightarrow 2(-1)^{\frac{5}{4}} \int_{0}^{\infty} w^{\frac{7}{2}} e^{-\left(\frac{w^2(-\gamma_i-1)}{2}\right)} \times I_{-\frac{1}{2}}\left(\sqrt{\frac{\mu^2\gamma_i}{\sigma^2}}jw\right) I_0\left(\sqrt{\frac{\upsilon^2}{\varrho^2}}jw\right)dw, \tag{15}$$

where $j = \sqrt{-1}$. The integral in (15) satisfies the identity given in [37, eq. 2.15.20.7] which leads to a closed-form expression as (16).

$$\int_{-\infty}^{0} f(z)dz = 4\sqrt{2}\left(\frac{\sigma^2}{\mu^2}\right)^{\frac{1}{4}} \sum_{k=0}^{\infty}(-1)^{-1-k}\frac{\Gamma(k+2)}{k!\Gamma(k+\frac{1}{2})} \left(\frac{\mu^2}{\sigma^2}\right)^{k} \frac{\gamma_i^{k-\frac{1}{4}}}{(\gamma_i+1)^{2k+2}} {}_2F_1\left(-k, \frac{1}{2}-k; 1; \frac{\upsilon^2\sigma^2}{\mu^2\varrho^2\gamma_i}\right), \quad \forall\ \gamma_i > 0. \tag{16}$$

We observe that $(-1)^{-1-k} = (-1)^{1+k}$ is an operator that subtract even values of k while adding odd values of k.

2) Part B: Let $w = \sqrt{z}$, we, therefore, have that $dz = 2wdw$ and $z = w^2$ with the integration boundary from 0 to ∞.

$$\int_{0}^{\infty} f(z)dz \Rightarrow 2\int_{0}^{\infty} w^{\frac{7}{2}} e^{-\left(\frac{w^2(\gamma_i+1)}{2}\right)} \times I_{-\frac{1}{2}}\left(\sqrt{\frac{\mu^2\gamma_i}{\sigma^2}}w\right) I_0\left(\sqrt{\frac{\upsilon^2}{\varrho^2}}w\right)dw. \tag{17}$$

Similarly, the integral in (17) satisfies the conditions given in [37, eq. 2.15.20.7] to obtain a closed-form expression for the integral as given in (18).

$$\int_{0}^{\infty} f(z)dz = 4\sqrt{2}\left(\frac{\sigma^2}{\mu^2}\right)^{\frac{1}{4}} \sum_{k=0}^{\infty}\frac{\Gamma(k+2)}{k!\Gamma(k+\frac{1}{2})} \left(\frac{\mu^2}{\sigma^2}\right)^{k} \frac{\gamma_i^{k-\frac{1}{4}}}{(\gamma_i+1)^{2k+2}} {}_2F_1\left(-k, \frac{1}{2}-k; 1; \frac{\upsilon^2\sigma^2}{\mu^2\varrho^2\gamma_i}\right), \quad \forall\ \gamma_i > 0. \tag{18}$$

Combining Part A and Part B of the integral, we have that

$$\int_{-\infty}^{\infty} f(z)dz = 4\sqrt{2}\left(\frac{\sigma^2}{\mu^2}\right)^{\frac{1}{4}} \sum_{k=0}^{\infty}\left(1+(-1)^{1+k}\right)\frac{\Gamma(k+2)}{k!\Gamma(k+\frac{1}{2})} \left(\frac{\mu^2}{\sigma^2}\right)^{k} \frac{\gamma_i^{k-\frac{1}{4}}}{(\gamma_i+1)^{2k+2}} {}_2F_1\left(-k, \frac{1}{2}-k; 1; \frac{\upsilon^2\sigma^2}{\mu^2\varrho^2\gamma_i}\right), \quad \forall\ \gamma_i > 0. \tag{19}$$

We observe that $1 + (-1)^{1+k}$ reduces the value of the summation to 0 when k is even but doubles the value when k is odd. This operation can be transformed by replacing k with $\kappa = 2k - 1$ while summing from $k = 1$ to ∞. Because κ is always a positive even number implies that $1+(-1)^{1+\kappa} = 2$. Therefore, by rearranging (19), collecting the terms of γ_i, and substituting $A(\gamma_i)$, we obtain (20) which can be simplified to Proposition 1. This completes the proof of the proposition.

$$p_\gamma(\gamma_i) = \frac{4\sqrt{2}e^{-\left(\frac{\mu^2}{2\sigma^2}+\frac{\upsilon^2}{2\varrho^2}\right)}}{\varrho\sigma^2} \sum_{k=1}^{\infty}\frac{\Gamma(\kappa+2)}{\kappa!\Gamma(\kappa+\frac{1}{2})} \left(\frac{\mu^2}{\sigma^2}\right)^{\kappa} \frac{\gamma_i^{\kappa-\frac{1}{2}}}{(\gamma_i+1)^{2\kappa+2}} {}_2F_1\left(-\kappa, \frac{1}{2}-\kappa; 1; \frac{\upsilon^2\sigma^2}{\mu^2\varrho^2\gamma_i}\right), \quad \forall\ \gamma_i > 0. \tag{20}$$

Remark 1: Since the first element of the hypergeometric function is a negative integer, the hypergeometric series is guaranteed to terminate thereby reducing to a polynomial [36], [38, eq. 9.101] [39, eq. 2.1.1.4], such that:

$${}_2F_1\left(-\kappa, \frac{1}{2}-\kappa; 1; \frac{\upsilon^2\sigma^2}{\mu^2\varrho^2\gamma_i}\right) = \sum_{m=0}^{\kappa}(-1)^m\binom{\kappa}{m}\frac{(\frac{1}{2}-\kappa)_m}{(1)_m}\left(\frac{\upsilon^2\sigma^2}{\mu^2\varrho^2\gamma_i}\right)^m, \quad \forall\ \left|\frac{\upsilon^2}{\varrho^2}\right| < \left|\frac{\mu^2}{\sigma^2}\gamma_i\right|, \tag{21}$$

where $\binom{\kappa}{m} = \frac{\kappa!}{m!(\kappa-m)!}$.

Remark 2: For $\gamma_i \leq 0$, $p_\gamma(\gamma_i) = 0$ since the $p_A(a)$ and $p_B(b)$ are equal to 0 for negative values. Since γ_i represents the signal-to-interference-noise-ratio (SINR) at specific i_{th} node, it is lower bound by zero while the physical environmental factors restrict its upper bound.

Corollary 1: Based on (9), the cumulative density function (CDF) of γ_i is given as (22).

$$F_{\gamma_i}(t) = \sum_{k=1}^{\infty}\sum_{m=0}^{\kappa} A_k(-1)^m\frac{\left(\frac{1}{2}-\kappa\right)_m}{(1)_m}\left(\frac{\upsilon^2\sigma^2}{\mu^2\varrho^2}\right)^m \times \frac{\kappa!}{m!(\kappa-m)!}\cdot\frac{t^{\kappa+\frac{1}{2}+m}}{(\kappa+\frac{1}{2}+m)} \times \left[{}_2F_1\left(2\kappa+2, \kappa+\frac{1}{2}+m; \kappa+\frac{3}{2}+m; -t\right) - B\left(\kappa+\frac{1}{2}+m, \kappa+\frac{3}{2}-m\right)\right], \quad \forall\ |\arg(1+t)| < \pi, \tag{22}$$

where $A_k = \frac{4\sqrt{2}e^{-\left(\frac{\mu^2}{2\sigma^2}+\frac{\upsilon^2}{2\varrho^2}\right)}\Gamma\left(\kappa+2\right)}{\kappa!\varrho\sigma^2\Gamma\left(\kappa+\frac{1}{2}\right)}\left(\frac{\mu^2}{\sigma^2}\right)^{\kappa}$, $\kappa = 2k-1$ and $(a)_m$ is the Pochhammer symbol (rising factorial) and is

presented as

$$(a)_m = \begin{cases} 1, & m = 0 \\ a(a+1)\dots(a+m-1) = \dfrac{\Gamma(a+m)}{\Gamma(a)}, & m > 0 \end{cases}$$

Proof: By definition of CDF, we have that $F_{\gamma_i}(t) = \int_{-\infty}^{t} p_\gamma(\gamma_i) d\gamma_i$. By substituting (9) into the definition of CDF, we obtain (23).

$$F_{\gamma_i}(t) = \sum_{k=1}^{\infty} A_k \int_{-\infty}^{t} \frac{\gamma_i^{\kappa-\frac{1}{2}}}{(\gamma_i+1)^{2\kappa+2}} {}_2F_1\left(-\kappa, \frac{1}{2}-\kappa; 1; \left(\frac{\upsilon^2\sigma^2}{\mu^2\varrho^2\gamma_i}\right)\right) d\gamma_i. \quad (23)$$

For simplification, by applying the transformation of [40, eq. 15.8.6] to the hypergeometric function and expanding with the terminating hypergeometric series definition presented in Remark 1, (23) can be re-written as (24).

$$F_{\gamma_i}(t) = \sum_{k=1}^{\infty}\sum_{m=0}^{\kappa} A_k(-1)^m \frac{\left(\frac{1}{2}-\kappa\right)_m}{(1)_m}\left(\frac{\upsilon^2\sigma^2}{\mu^2\varrho^2}\right)^m \frac{\kappa!}{m!(\kappa-m)!}\int_{-\infty}^{t}\frac{\gamma_i^{\kappa-\frac{1}{2}+m}}{(\gamma_i+1)^{2\kappa+2}}d\gamma_i. \quad (24)$$

We note that

$$\int_{-\infty}^{t} f(\gamma_i)d\gamma_i = \underbrace{\int_{-\infty}^{0} f(\gamma_i)d\gamma_i}_{Part\ A} + \underbrace{\int_{0}^{t} f(\gamma_i)d\gamma_i}_{Part\ B},$$

where $f(\gamma_i) = \frac{\gamma_i^{\kappa-\frac{1}{2}+m}}{(\gamma_i+1)^{2\kappa+2}}$.

1) Part A: Let $w = -\gamma_i$, therefore, $dw = -d\gamma_i$ with integration boundary from ∞ to 0. However, if we rearrange the equations, we obtain the left-hand section of (25) with solution from [38, 3.194.3].

$$(-1)^{\kappa-\frac{1}{2}+m}\int_0^{\infty}\frac{(w)^{\kappa-\frac{1}{2}+m}}{(-w+1)^{2\kappa+2}}dw = -B\left(\kappa+\frac{1}{2}+m, \kappa+\frac{3}{2}-m\right), \quad (25)$$

where B represents a beta function.

2) Part B: The integral of Part B satisfies the identity given in [38, 3.194.2]

$$\int_0^t \frac{\gamma_i^{\kappa-\frac{1}{2}+m}}{(\gamma_i+1)^{2\kappa+2}}d\gamma_i = \frac{t^{\kappa+\frac{1}{2}+m}}{(\kappa+\frac{1}{2}+m)} \times {}_2F_1\left(2\kappa+2, \kappa+\frac{1}{2}+m; \kappa+\frac{3}{2}+m; -t\right), \quad \forall\,|\arg(1+t)| < \pi, \quad (26)$$

We can solve the integral in (24) by obtaining Part A and B. Therefore, we get the CDF given in Corollary 1 by substituting their solutions to the integral and simplifying further to obtain (22). The conditions for the validity of (22) hold for real values of $t \geq -1$. However, recall that t represents the SINR which is a positive parameter, the acceptable t values will be $t \geq 0$. That completes the proof.

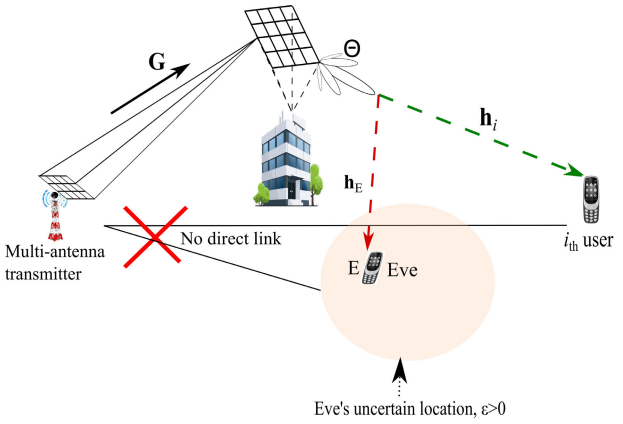

FIGURE 4. Applying the SINR density distribution in determining the average secrecy rate.

VI. APPLICATION OF THE SINR DENSITY DISTRIBUTION

In this section, we apply the derived SINR PDF presented in (9) to obtain the average secrecy rate formulation and show that the CDF defined in (23) is essential in determining the outage probability. We note that a detailed discussion about the average secrecy rate formula is available in [20], however, we focus mainly on the use-case of this paper which emphasizes the application of the SINR densities. Let us consider a 6G spectrum scenario where the SINR density distribution is used to determine the average secrecy rate of the transmission. In Fig. 4, a passive eavesdropper (Eve) attempts to listen to the communication between the transmitter and the legitimate i_{th} user through the IRS reflection path. The 6G physical layer transmission path is configured with settings from [41]. It has been established in [42] that characterizing the density distributions is useful in determining performance metrics like the outage probability and the average secrecy rate.

1) OUTAGE PROBABILITY

The outage probability defines the probability that the information content may go below a specified threshold given varying channel characteristics. By definition, the model to determine the outage probability is the same as the CDF presented in Corollary 1 when the threshold (t) is set according to channel conditions.

$$P_{outage}(\gamma \leq t) = F_\gamma(t).$$

2) AVERAGE SECRECY RATE

Let us consider that the SINR of a legitimate and an illegitimate receiver is γ_b and γ_e respectively with a density distribution function, $p_\gamma(\gamma_i)\ \forall\ i \in \{b,\ e\}$, and giving rise to

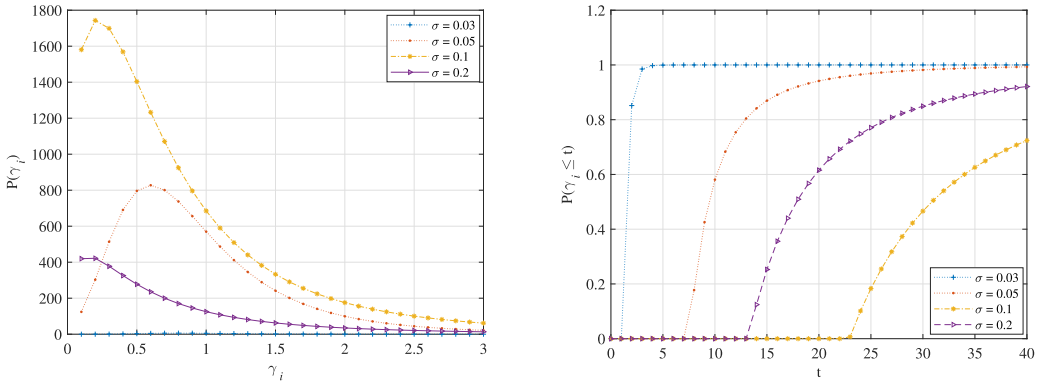

a PDF b CDF

FIGURE 5. Effect of the fading parameter (σ) of the desired signal on the SINR distribution.

an average secrecy rate defined in (27) [20].

$$R_s = \int_0^{\gamma_b} \left[\log_2(1+\gamma_b) - \log_2(1+\gamma_e)\right] p_\gamma(\gamma_e) d\gamma_e. \quad (27)$$

$$R_s = \ln(1+\gamma_b) \underbrace{\int_0^{\gamma_b} p_\gamma(\gamma_e) d\gamma_e}_{\text{Part A}} - \underbrace{\int_0^{\gamma_b} \ln(1+\gamma_e) p_\gamma(\gamma_e) d\gamma_e}_{\text{Part B}}. \quad (28)$$

The solution to the integral of part A of (28) is the same as the CDF given in (22) of corollary 1 by replacing t with γ_b. Let $f(\gamma_e) = \ln(1+\gamma_e)p_\gamma(\gamma_e)$ and $\ln(1+z) = z\,{}_2F_1(1,1;2;-z)$ from [38, eq. 9.121.6], we find the integral of part B is (29) as

$$\int_0^{\gamma_b} f(\gamma_e) d\gamma_e = \sum_{k=1}^{\infty} A_k \int_0^{\gamma_b} \frac{\gamma_e^{\kappa+\frac{1}{2}}}{(\gamma_e+1)^{2\kappa+2}} \times {}_2F_1\left(-\kappa, \frac{1}{2}-\kappa; 1; \frac{\upsilon^2\sigma^2}{\mu^2\varrho^2\gamma_e}\right) {}_2F_1(1,1;2;-\gamma_e) d\gamma_e. \quad (29)$$

Since the product of 2 Gauss hypergeometric functions was given in [39, eq. 4.3(14)] and [43, eq. 44(7.2.3)], (29) can be expressed as (30).

$$\int_0^{\gamma_b} f(\gamma_e) d\gamma_e = \sum_{k=1}^{\infty}\sum_{m=0}^{\infty} A_k Q_k \times {}_4F_3\left(1,1,\frac{1}{2}-m,-m;2,\frac{1}{2}-k-m,\frac{1}{2}-k-m;\left(-\frac{\mu^2\varrho^2}{\upsilon^2\sigma^2}\right)\right) \times \int_0^{\gamma_b} \frac{\gamma_e^{\frac{1}{2}+m}\left(\frac{\upsilon^2\sigma^2}{\mu^2\varrho^2}-\gamma_e\right)^{2k+\frac{1}{2}}}{(\gamma_e+1)^{2\kappa+2}} d\gamma_e, \quad (30)$$

where $Q_k = \frac{((\frac{1}{2}+k)_m)^2\left(\frac{\upsilon^2\sigma^2}{\mu^2\varrho^2}\right)^{-m-k-\frac{1}{2}}(\frac{1}{2}-k)_k}{(-1)^k(1)_k m!(\frac{1}{2})_m}$. The integral in (30) can be obtained from [38, eq. 3.197.8] leading the expression for the Part B of (28) to becoming (31).

$$\int_0^{\gamma_b} f(\gamma_e) d\gamma_e = \sum_{k=1}^{\infty}\sum_{m=0}^{\infty} A_k Q_k \times {}_4F_3\left(1,1,\frac{1}{2}-m,-m;2,\frac{1}{2}-k-m,\frac{1}{2}-k-m;\left(-\frac{\mu^2\varrho^2}{\upsilon^2\sigma^2}\right)\right) \times \gamma_b^{2k+m+2} B\left(2k+\frac{3}{2},\frac{3}{2}+m\right) \times {}_2F_1\left(-2k-2,\frac{3}{2}+m;2k+3+m;-\gamma_b\right) d\gamma_e. \quad (31)$$

Having obtained the integrals for Part A and B of (28), a generalized average secrecy rate expression given in (32), as shown at the bottom of the next page, was derived.

VII. ANALYSIS AND DISCUSSION

The PDF and CDF of the SINR given in (9) and (22) respectively were evaluated in figures 5 to 7 by varying the location and shape parameters. Table 1 gives the values of key parameters used to generate the figures unless otherwise stated without loss of generality. The simulation parameters highlighted in this paper were determined to provide excerpts of the results discussed herein. However, other values that obey the boundary constraints discussed in the preceding sections will produce valid and similar results.

Figure 5 presents the PDF and CDF of the SINR when the scale parameter σ was varied. We recall that σ is a property of the desired signal density distribution characterising its fading coefficient. We observe that by varying σ, the shape of the SINR distribution changes, defined by its characteristic.

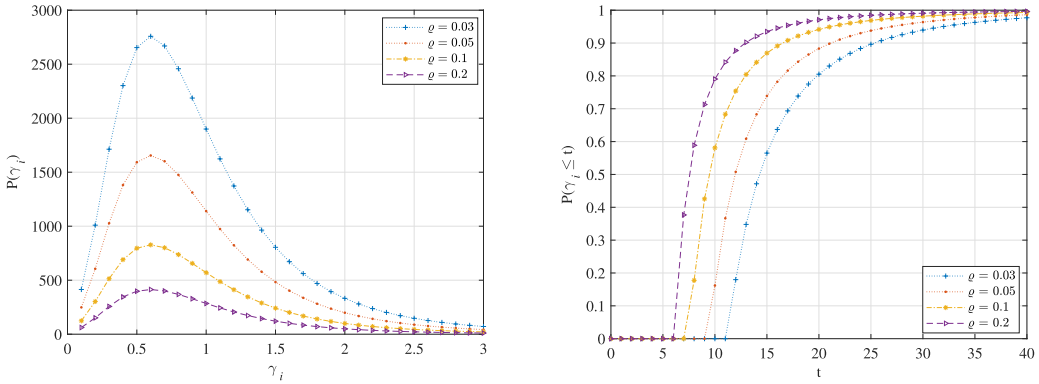

a. PDF b. CDF

FIGURE 6. Impact of varying the interfering signal fading parameter (ϱ) on the SINR distribution.

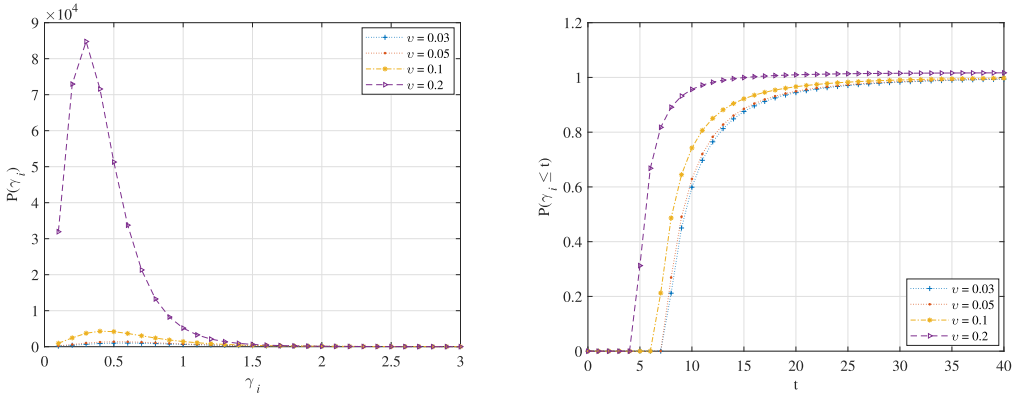

a. PDF b. CDF

FIGURE 7. Impact of varying the interfering signal power (υ) coefficient on the SINR distribution.

There are no observable patterns to the varying σ because it relies directly on the random channel characteristics between the transmitter, IRS and receiver. However, compared with Figs. 6 and 7, the impact of varying the desired signal parameter is significantly larger than that of the interfering signal. We recall from (8), that the scale parameter for the desired signal is lower bound by zero (i.e. $\sigma > 0$), therefore as $\sigma \to 0$, the desired signal is attenuated and distribution fades. This accounts for the observation in Fig. 5 where the PDF approaches zero as $\sigma \to 0$.

Figures 6 and 7 present the influence of the interfering signals on the SINR of the IRS-based communication system. In both figures, we vary the fading coefficients of the interfering signals and their power by increasing ϱ and υ respectively. We observe that reducing these parameters drives the SINR distribution to become Rayleigh distributed. For example, for $\upsilon = 0$, the expression ${}_2F_1\big(-\kappa, \frac{1}{2} - \kappa; 1; 0\big) = 1$ [43, eq. 8 (7.2.3)], which causes the SINR PDF to become the sum of a scaled Rayleigh distribution. This validates the report in [25] that the SNR becomes Rayleigh

$$R_s = \sum_{k=1}^{\infty} A_k \Bigg[\ln(1+\gamma_b) \sum_{m=0}^{\kappa} (-1)^m \frac{\left(\frac{1}{2}-\kappa\right)_m}{(1)_m} \left(\frac{\upsilon^2\sigma^2}{\mu^2\varrho^2}\right)^m \frac{\kappa!}{m!(\kappa-m)!} \cdot \frac{\gamma_b^{\kappa+\frac{1}{2}+m}}{(\kappa+\frac{1}{2}+m)}$$
$$\times \left({}_2F_1\left(2\kappa+2, \kappa+\frac{1}{2}+m; \kappa+\frac{3}{2}+m; -\gamma_b\right) - B\left(\kappa+\frac{1}{2}+m, \kappa+\frac{3}{2}-m\right)\right)\Bigg] - \Bigg[\sum_{m=0}^{\infty} (-1)^m \frac{((1)_m)^2 \gamma_b^{\kappa+\frac{3}{2}+m}}{m!(2)_m(\kappa+\frac{3}{2}+m)}$$
$$\times {}_4F_3\left(-\kappa, \frac{1}{2}-\kappa, -1-m, -m; 1, -m, -m; \left(-\frac{\mu^2\varrho^2}{\upsilon^2\sigma^2}\right)\right) {}_2F_1\left(2\kappa+2, \kappa+\frac{3}{2}+m; \kappa+\frac{5}{2}+m; -\gamma_b\right)\Bigg] \tag{32}$$

TABLE 1. Simulation/Testing Parameters.

Simulation parameter	Symbol	Value
Desired signal scale	σ	0.05
Desired signal location	μ	0.2
Interfering signal scale	ϱ	0.1
Interfering signal location	υ	0
Transmission Frequency	f	300 GHz

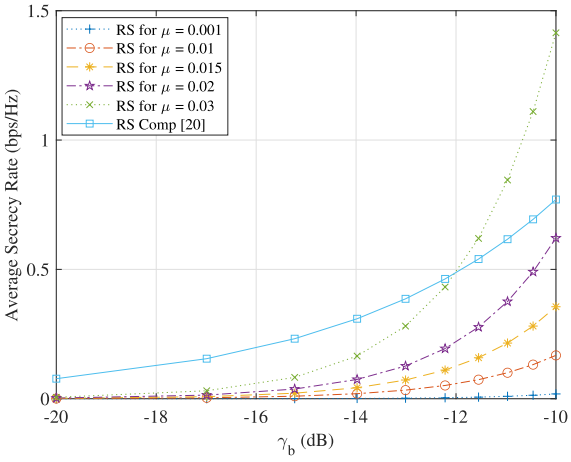

FIGURE 8. Varying the legitimate power (μ) while evaluating average secrecy rate against desired SNR at $\upsilon = 0.01$, $\sigma = 0.1$, $\varrho = 0.05$.

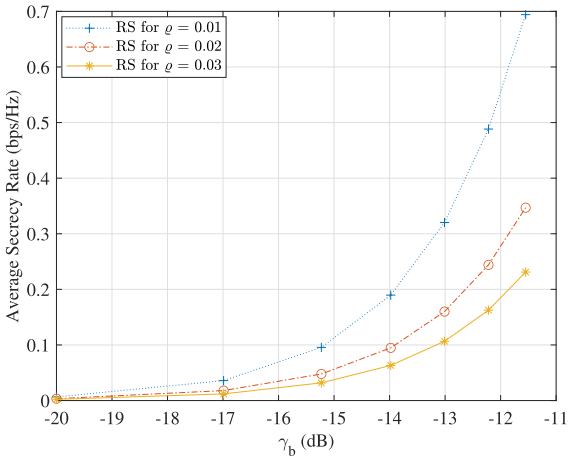

FIGURE 9. Impact of varying (ϱ) while evaluating average secrecy rate against desired SNR at $\upsilon = 0.01$, $\sigma = 0.1$, $\mu = 0.01$.

distributed if interference is not considered.

$$p_\gamma(\gamma_i) = \sum_{k=1}^{\infty} \frac{4\sqrt{2}e^{-\frac{\mu^2}{2\sigma^2}}\Gamma\left(\kappa+2\right)}{\kappa!\varrho\sigma^2\Gamma\left(\kappa+\frac{1}{2}\right)}\left(\frac{\mu^2}{\sigma^2}\right)^{\kappa}\frac{\gamma_i^{\kappa-\frac{1}{2}}}{(\gamma_i+1)^{2\kappa+2}}$$

Specifically, for Fig. 6a, increasing the location parameter which defines the effect of the fading channel on the interfering signal decreases the amplitude of the PDF while increasing the likelihood of the SINR probability falling below a threshold. We observe from Fig. 7a that reducing the interfering signal power coefficient reduces the amplitude of the PDF and vice versa. Similarly, from Fig. 7b, the reduced power coefficient increases the likelihood that the probability of the SINR value is below a threshold.

Furthermore, Figs. 8 and 9 show the application of the SINR density distribution function in determining the average secrecy rate for passive eavesdropping. Using the same benchmark network, Fig. 8 showed a similar exponential trend when compared to the average secrecy rate computation derived in [20]. However, increasing the legitimate signal power (μ) improves the average secrecy rate. The higher μ values allow the IRS system to focus the transmission to the desired location, thereby limiting eavesdropping. Similarly, Fig. 9 presents the impact of varying the interfering signal scale (ϱ) on the average secrecy rate. Increasing ϱ improves the average secrecy rate. This is because the scale parameter, ϱ, represents the variability of the interfering signal distribution. Therefore, larger ϱ spreads out the distribution of the interfering signal ensuring focused legitimate signal distribution.

VIII. CONCLUSION AND RECOMMENDATION

We have presented an analytical derivation of the PDF and CDF of the SINR from a system comprising a 6G transmitting station through an IRS system to a ground-based receiver. From the results, we note that the PDF of the IRS-based SINR contains a hypergeometric function and is influenced by the fading coefficients of the desired and interfering signals. The core metrics of the density function depend on the weighted average of the superposition of the signals from the IRS elements. This knowledge is essential as it allows the realistic statistical modelling of the received signals applicable to data rate determination and physical layer security. We demonstrated this application by evaluating the average secrecy rate metric for a typical physical layer security system. We anticipate that the density distribution will be valuable in defining the transition state space probability models for training machine learning algorithms to configure the phase shifts of the IRS system.

LIST OF ABBREVIATIONS

5G	Fifth Generation.
6G	Sixth Generation.
AI	Artificial Intelligence.
AWGN	Additive White Gaussian Noise.
BER	Bit Error Rate.
CDF	Cumulative Distribution Function.
CCI	Co-Channel Interference.
CLT	Central Limit Theory.
GHz	Giga Hertz.
gNB	Next Generation Node B.
IRS	Intelligent Reflecting Surfaces.
LoS	Line of Sight.
MISO	Multiple Input Single Output.
NLoS	Non-Line of Sight.

NOMA	Non-Orthogonal Multiple Access.
ORAN	Open Radio Access Network.
PDF	Probability Density Function.
SINR	Signal-to-Interference Noise Ratio.
SISO	Single Input Single Output.
SNR	Signal-to-Noise Ratio.
THz	Tera Hertz.
QoS	Quality of Service.
RAN	Radio Access Network.
RIC	RAN Intelligent Controller.
UAV	Unmmanned Aerial Vehicle.

ACKNOWLEDGMENT

REFERENCES

[1] X. Liu, H. Zhang, M. Sheng, W. Li, S. Al-Rubaye, and K. Long, "Ultra dense satellite-enabled 6G networks: Resource optimization and interference management," *China Commun.*, vol. 20, no. 10, pp. 262–275, Oct. 2023.

[2] A. Warrier, L. Aljaburi, H. Whitworth, S. Al-Rubaye, and A. Tsourdos, "Future 6G communications powering vertical handover in non-terrestrial networks," *IEEE Access*, vol. 12, pp. 33016–33034, 2024.

[3] S. Al-Rubaye, C. Conrad, and A. Tsourdos, "Communication network architecture with 6G capabilities for urban air mobility," in *Proc. IEEE Int. Conf. Consum. Electron. (ICCE)*, Jan. 2024, pp. 1–6.

[4] K. Mohanta and S. Al-Rubaye, "Towards 6G satellite–terrestrial networks: Analysis of air mobility operations," *Electronics*, vol. 13, no. 14, p. 2855, Jul. 2024.

[5] W. Wang and W. Zhang, "Intelligent reflecting surface configurations for smart radio using deep reinforcement learning," *IEEE J. Sel. Areas Commun.*, vol. 40, no. 8, pp. 2335–2346, Aug. 2022.

[6] Y. Zhou, Z. Jin, H. Shi, L. Shi, and N. Lu, "Flying IRS: QoE-driven trajectory optimization and resource allocation based on adaptive deployment for WPCNs in 6G IoT," *IEEE Internet Things J.*, vol. 11, no. 5, pp. 9031–9046, Mar. 2024.

[7] S. A. H. Mohsan, M. A. Khan, M. H. Alsharif, P. Uthansakul, and A. A. A. Solyman, "Intelligent reflecting surfaces assisted UAV communications for massive networks: Current trends, challenges, and research directions," *Sensors*, vol. 22, no. 14, p. 5278, Jul. 2022.

[8] C. O. Nnamani, M. R. A. Khandaker, and M. Sellathurai, "Secure data collection via UAV-carried IRS," *ICT Exp.*, vol. 9, no. 4, pp. 706–713, Aug. 2023.

[9] Y. Gao, Y. Zhang, H. Geng, X. Li, D. B. Da Costa, and M. Zeng, "Aerial-IRS-assisted securing communications against eavesdropping: Joint trajectory and resource allocation," *IEEE Internet Things J.*, vol. 11, no. 7, pp. 11974–11985, Apr. 2024.

[10] D. Wang, X. Li, M. Wu, Y. He, Y. Lou, Y. Pang, and Y. Lu, "Secure intelligent reflecting surface assisted mobile edge computing system with wireless power transfer," *Digit. Commun. Netw.*, vol. 10, no. 6, pp. 1874–1880, Dec. 2024.

[11] E. E. Haber, M. Elhattab, C. Assi, S. Sharafeddine, and K. K. Nguyen, "Multi-IRS aided mobile edge computing for high reliability and low latency services," *IEEE Trans. Netw. Service Manage.*, vol. 21, no. 4, pp. 4396–4409, Aug. 2024.

[12] X. Shao, C. You, W. Ma, X. Chen, and R. Zhang, "Target sensing with intelligent reflecting surface: Architecture and performance," *IEEE J. Sel. Areas Commun.*, vol. 40, no. 7, pp. 2070–2084, Jul. 2022.

[13] M. Hua, Q. Wu, W. Chen, Z. Fei, H. C. So, and C. Yuen, "Intelligent reflecting surface-assisted localization: Performance analysis and algorithm design," *IEEE Wireless Commun. Lett.*, vol. 13, no. 1, pp. 84–88, Jan. 2024.

[14] D. Dampahalage, K. B. S. Manosha, N. Rajatheva, and M. Latva-aho, "Intelligent reflecting surface aided vehicular communications," in *Proc. IEEE Globecom Workshops (GC Wkshps*, Dec. 2020, pp. 1–6.

[15] M. Danger, S. Häger, K. Heimann, S. Böcker, and C. Wietfeld, "Empowering 6G industrial indoor networks: Hands-on evaluation of IRS-enabled multi-user mmWave connectivity," in *Proc. Joint Eur. Conf. Netw. Commun. 6G Summit (EuCNC/6G Summit)*, Jun. 2024, pp. 949–954.

[16] K. Ikeagu, M. R. A. Khandaker, C. Song, and Y. Ding, "Deep learning-based hybrid beamforming design for IRS-aided MIMO communication," *IEEE Wireless Commun. Lett.*, vol. 13, no. 2, pp. 461–465, Feb. 2024.

[17] M. Munawar, M. Guenach, and I. Moerman, "Machine vision aided adaptive beamforming decision for IRS-assisted wireless networks," in *Proc. Joint Eur. Conf. Netw. Commun. 6G Summit (EuCNC/6G Summit)*, Jun. 2024, pp. 517–522.

[18] F. C. Okogbaa, Q. Z. Ahmed, F. A. Khan, W. B. Abbas, F. Che, S. A. R. Zaidi, and T. Alade, "Design and application of intelligent reflecting surface (IRS) for beyond 5G wireless networks: A review," *Sensors*, vol. 22, no. 7, p. 2436, Mar. 2022.

[19] Z. Cui, K. Guan, J. Zhang, and Z. Zhong, "SNR coverage probability analysis of RIS-aided communication systems," *IEEE Trans. Veh. Technol.*, vol. 70, no. 4, pp. 3914–3919, Apr. 2021.

[20] C. O. Nnamani, M. R. A. Khandaker, and M. Sellathurai, "UAV-aided jamming for secure ground communication with unknown eavesdropper location," *IEEE Access*, vol. 8, pp. 72881–72892, 2020.

[21] D. L. Sharini, R. Dilli, M. Kanthi, and G. D. Goutham Simha, "Channel modeling for IRS-assisted MIMO systems to analyze the effects of nonlinear distortions in wireless environments," *IEEE Access*, vol. 12, pp. 84216–84225, 2024.

[22] A. Danish, S. Ali, M. I. Aslam, and I. Ahmed, "Future prospects and challenges associated with intelligent reflecting surfaces enabled wireless communication," in *Proc. IEEE 18th Int. Conf. Smart Communities, Improving Quality Life Using ICT, IoT AI (HONET)*, Oct. 2021, pp. 121–125.

[23] Y. Liu, I. Al-Nahhal, O. A. Dobre, and F. Wang, "Deep-learning channel estimation for IRS-assisted integrated sensing and communication system," 2024, *arXiv:2402.09441*.

[24] S. Almaghthawi, E. Alsusa, and A. Al-Dweik, "On the performance of IRS-aided NOMA in interference-limited networks," *IEEE Wireless Commun. Lett.*, vol. 13, no. 2, pp. 560–564, Feb. 2024.

[25] W. Tan, Q. Zhou, W. Tan, L. Yang, and C. Li, "Performance analysis of intelligent reflecting surface assisted wireless communication system," *Comput. Model. Eng. Sci.*, vol. 137, no. 1, pp. 775–787, 2023.

[26] D. L. Galappaththige, D. Kudathanthirige, and G. Amarasuriya, "Performance analysis of distributed intelligent reflective surface aided communications," in *Proc. GLOBECOM-IEEE Global Commun. Conf.*, Dec. 2020, pp. 1–6.

[27] W. Aman, M. M. Ur Rahman, S. Ansari, A. A. Nasir, K. Qaraqe, M. A. Imran, and Q. H. Abbasi, "On the effective capacity of IRS-assisted wireless communication," *Phys. Commun.*, vol. 47, Aug. 2021, Art. no. 101339.

[28] Ö. Özdogan, E. Björnson, and E. G. Larsson, "Intelligent reflecting surfaces: Physics, propagation, and pathloss modeling," *IEEE Wireless Commun. Lett.*, vol. 9, no. 5, pp. 581–585, May 2020.

[29] M. Cui, G. Zhang, and R. Zhang, "Secure wireless communication via intelligent reflecting surface," *IEEE Wireless Commun. Lett.*, vol. 8, no. 5, pp. 1410–1414, Oct. 2019.

[30] H. Lu, Y. Zeng, S. Jin, and R. Zhang, "Aerial intelligent reflecting surface: Joint placement and passive beamforming design with 3D beam flattening," *IEEE Trans. Wireless Commun.*, vol. 20, no. 7, pp. 4128–4143, Jul. 2021.

[31] S. Li, B. Duo, M. D. Renzo, M. Tao, and X. Yuan, "Robust secure UAV communications with the aid of reconfigurable intelligent surfaces," *IEEE Trans. Wireless Commun.*, vol. 20, no. 10, pp. 6402–6417, Oct. 2021.

[32] Q. Wu and R. Zhang, "Intelligent reflecting surface enhanced wireless network: Joint active and passive beamforming design," in *Proc. IEEE Global Commun. Conf. (GLOBECOM)*, Dec. 2018, pp. 1–6.

[33] L. Ge, P. Dong, H. Zhang, J.-B. Wang, and X. You, "Joint beamforming and trajectory optimization for intelligent reflecting surfaces-assisted UAV communications," *IEEE Access*, vol. 8, pp. 78702–78712, 2020.

[34] H. Ibrahim, H. Tabassum, and U. T. Nguyen, "Exact coverage analysis of intelligent reflecting surfaces with nakagami-m channels," 2021, *arXiv:2101.00740*.

[35] (2001). *The Wolfram Functions Site. BesselI Function*. Accessed: Sep. 10, 2021. [Online]. Available: http://functions.wolfram.com/03.02.03.0005.01

[36] *Hypergeometric Function*. Accessed: Sep. 10, 2021. [Online]. Available: https://en.wikipedia.org/wiki/Hypergeometric_function
[37] A. P. Prudnikov, Y. A. Brychkov, and O. I. Marichev, *Integrals and Series*, vol. 2. New York, NY, USA: Gordon & Breach, 1986.
[38] I. S. Gradshteyn and I. M. Ryzhik, *Table of Integrals, Series and Products*, 7th ed., A. Jeffrey and D. Zwillinger, Eds., New York, NY, USA: Academic, 2007.
[39] A. Erdelyi, *Higher Transcendental Functions*, vol. 1. New York, NY, USA: McGraw-Hill, 1953.
[40] F. W. J. Olver, A. B. O. Daalhuis, D. W. Lozier, B. I. Schneider, R. F. Boisvert, C. W. Clark, B. R. Miller, B. V. Saunders, H. S. Cohl, and M. A. McClain. *Nist Digital Library of Mathematical Functions*. Accessed: Sep. 22, 2021. [Online]. Available: http://dlmf.nist.gov/
[41] M. Matthaiou, O. Yurduseven, H. Q. Ngo, D. Morales-Jimenez, S. L. Cotton, and V. F. Fusco, "The road to 6G: Ten physical layer challenges for communications engineers," *IEEE Commun. Mag.*, vol. 59, no. 1, pp. 64–69, Jan. 2021.
[42] I. Trigui, W. Ajib, and W.-P. Zhu, "Secrecy outage probability and average rate of RIS-aided communications using quantized phases," *IEEE Commun. Lett.*, vol. 25, no. 6, pp. 1820–1824, Jun. 2021.
[43] A. P. Prudnikov, Y. A. Brychkov, and O. I. Marichev, *Integrals and Series*, vol. 3. New York, NY, USA: Gordon & Breach, 1986.

CHRISTANTUS OBINNA NNAMANI (Member, IEEE) received the B.Eng. degree in electronic engineering and the M.Eng. and Ph.D. degrees in electronic engineering (telecommunications) from the University of Nigeria, Nsukka, in 2011, 2015, and 2021 respectively, and the Ph.D. degree from the School of Engineering and Physical Sciences, Heriot-Watt University, Edinburgh, U.K., in 2022. He is currently a Senior Research and Development Engineer with PNDC, University of Strathclyde. He is an experienced Researcher with over ten years of career experience working with university research groups and industrial partners. He consulted for EarSwitch Ltd., DSTL, and the Centre Tecnológic de les Telecomunicacions de Catalunya (CTTC), Spain, on ultrasound, radar, and small satellite deployment projects. He worked on three U.K., future flight three projects—Blueprint, HADO, and AMEC and researched digital twinning for 6G under the UKRI CHEDDAR Project at Cranfield University. His research interests include UAV, UTM, ATM, NGN, network security, resource allocation, digital twinning, virtualization, simulation, and modeling. He was awarded the Petroleum Technology Development Fund (PTDF), Nigeria overseas Ph.D. sponsorship in 2018, and also an Erasmus Mobility Student (under the DREAM Project ACP-18) at the Universitá degli Studi di Cagliari, Italy, from 2015 to 2016.

CHIDERA LINDA ANIOKE received the B.Eng. degree (Hons.) in electrical and electronic engineering from Nnamdi Azikiwe University, Awka, Nigeria, in 2008, and the M.Eng. and Ph.D. degrees in communication engineering from the University of Nigeria, Nsukka, in 2015 and 2019, respectively. She is currently a Senior Lecturer with the Department of Electronic and Computer Engineering, University of Nigeria, with many years of experience in teaching and research. She was the LMC Representative of Electronic Engineering for the Intra Africa Academic Mobility Program on Computer Engineering Education in Africa (AFRICOM Project). Her research interests include UAV, network security, channel resource allocation, and signal processing. She is also a Corporate Member of the Council for the Regulation of Engineering in Nigeria (COREN).

SABA AL-RUBAYE (Life Senior Member, IEEE) is currently a Professor Chair of telecommunications and autonomous systems with the Centre for Autonomous and Cyberphysical Systems, Cranfield University, U.K. She is leading and involved with several projects, including Cheddar-EPSRC, HADO-Innovate U.K., Rise—Innovate U.K., UAS Authentication Service-Innovate U.K., and Aviation Innovation in South-West-Innovate U.K., H2020 SESAR AMULED, and DfT–Smart Airport, to design new techniques, and integrated software/hardware hub proof of concept. She has published many papers in IEEE journals and conferences. She is participating in developing industry standards by being an Active Research Group Member of the IEEE P1932.1 Standard of License/Unlicensed Interoperability and IEEE P1920.2 Standard for Vehicle-to-Vehicle Communications for Unmanned Aircraft Systems. She is a member of the Institute of Engineering and Technology (IET) and registered as a Chartered Engineer (C.Eng.). She has delivered tutorials at IEEE ICC, IEEE WCNC, and IEEE VTC conferences; and invited talks at various venues, including the Communications Research Centre (CRC) of Canada, IEEE Toronto Chapter, and IEEE U.K. Chapter. She was a recipient of the Best Technical Paper Award (twice) published in IEEE Vehicular Technology, in 2011 and 2015, respectively. She has been the general co-chair and the TPC co-chair and has held other leading roles at many international conferences.

ANTONIOS TSOURDOS received the M.Eng. degree in electronic, control and systems engineering from the University of Sheffield, in 1995, the M.Sc. degree in systems engineering from Cardiff University, in 1996, and the Ph.D. degree in nonlinear robust flight control design and analysis from Cranfield University, in 1999. He was appointed as the Head of the Autonomous Systems Group, Cranfield Defence and Security, in 2007, and the Centre of Autonomous and Cyber-Physical Systems, School of Aerospace, Transport and Manufacturing in 2012, and the Director of the Research—Aerospace, Transport and Manufacturing, in 2015. He is currently a Professor of autonomous systems and control with Cranfield University. He was a member of Team Stellar, the winning team for the U.K. MoD Grand Challenge (2008) and the IET Innovation Award (Category Team, 2009). He was a member of the BSI Future Flight Standards Hub (2023–2024) and the AIAA Advanced Aerial Mobility Certification Task Force (2023–2024). He is a fellow of the Royal Aeronautical Society. He served as the chair for the IFAC Technical Committee on Aerospace Control (2017–2023).